

High-resolution Rayleigh wave slowness tomography of central Asia

Mónica Maceira,^{1,2} Steven R. Taylor,¹ Charles J. Ammon,² Xiaoning Yang,¹
and Aaron A. Velasco³

Received 13 September 2004; revised 19 January 2005; accepted 14 March 2005; published 9 June 2005.

[1] We compute short-period, high-resolution surface wave slowness maps for central Asia using Bayesian tomography. We focus on the region between 69° and 108°E and 29° and 54°N and used seismograms from more than 1100 events. Using multiple-filter and phase-matched filter techniques, we measured the dispersion characteristics of the signals between 6 and 30 s period. These Rayleigh wave group velocity dispersion curves were used to compute high-resolution, half-degree cell size, slowness tomographic maps. Because short periods are primarily sensitive to upper crustal structures, the images display low velocities associated with the Tarim, Junggar, and Qaidam basins. Relatively high velocities are associated with mountainous tectonic features such as the Tian Shan. We validated our maps using dispersion curves from 640 events that were not used to construct the tomographic model. The model predictions show a significant variance reduction at short and intermediate periods (6–15 s) with respect to the prior model. Our model also shows 15% improvement in surface wave detection capability with respect to previous one-dimensional models. These high-resolution, short-period tomography maps can help improve regional magnitude estimations for construction of $m_b:M_s$ discriminants. Moreover, the short-period surface wave tomographic results show unprecedented resolution that reveals greater geologic detail than has previously been achieved using surface waves and that give us insight into the shear velocity structure of the crust underlying this part of Asia.

Citation: Maceira, M., S. R. Taylor, C. J. Ammon, X. Yang, and A. A. Velasco (2005), High-resolution Rayleigh wave slowness tomography of central Asia, *J. Geophys. Res.*, 110, B06304, doi:10.1029/2004JB003429.

1. Introduction

[2] Surface waves have long been used to study the Earth's shear velocity structure and to monitor nuclear explosions with discriminants such as body, m_b , to surface wave, M_s , magnitude ratios. Surface waves exhibit a frequency-dependent sensitivity to crustal and mantle structure as they propagate along the Earth's surface, causing the wave trains to disperse. By measuring the dispersion of surface waves, average one-dimensional (1-D) velocity models can be developed along a great circle path. Surface wave dispersion studies were abundant during the 1950s and 1960s [see Ewing *et al.*, 1957; Oliver, 1962; Dziewonski, 1971; Knopoff, 1972]. With the installation of the World Wide Standardized Seismograph Network (WWSSN) in the 1960s, surface waves became one of the primary sources for investigating the deeper part of the crust and the upper mantle [e.g., Patton, 1980; Pines *et al.*, 1980; Romanowicz, 1982; Wier, 1982; Feng and Teng, 1983; Brandon and Romanowicz, 1986; Bourjot and Romanowicz, 1992]. The

resolution of these earlier studies was limited due to the scarcity of the seismic stations and the quality of the data. With the significant development of the Global Seismic Network (GSN) [Butler *et al.*, 2004] and computing power, classical dispersion studies can be extended to include tomographic methods for large number of surface wave dispersion measurements over large areas [e.g., Levshin *et al.*, 2001b; Godey *et al.*, 2003].

[3] Central Asia has been the subject of numerous geophysical studies because of its significance to the understanding of the formation and evolution of the continents. In particular, there have been a number of surface wave dispersion studies across this area [e.g., Chen and Molnar, 1975; Bird and Tököz, 1977; Jobert *et al.*, 1985; Levshin *et al.*, 1992, 1994; Levshin and Ritzwoller, 1995; Curtis and Woodhouse, 1997]. Wu *et al.* [1997] presented a Rayleigh wave group velocity model of Siberia, China, and vicinity areas for periods between 30 and 70 s. Ritzwoller and Levshin [1998] computed Rayleigh and Love wave group velocity maps on a large spatial scale (all of Eurasia) and for a broad period band (20–200 s). Ritzwoller *et al.* [1998] presented a study of intermediate-period (10–40 s) Rayleigh and Love wave dispersion across central Asia, western China, and parts of the Middle East. More recently, Huang *et al.* [2003] published the result of a Rayleigh wave tomography study of China and neighboring regions for periods between 10 and 184 s. In general, the resulting tomographic images of these studies agree well with each

¹Los Alamos National Laboratory, Los Alamos, New Mexico, USA.

²Department of Geosciences, Pennsylvania State University, University Park, Pennsylvania, USA.

³Department of Geological Sciences, University of Texas at El Paso, El Paso, Texas, USA.

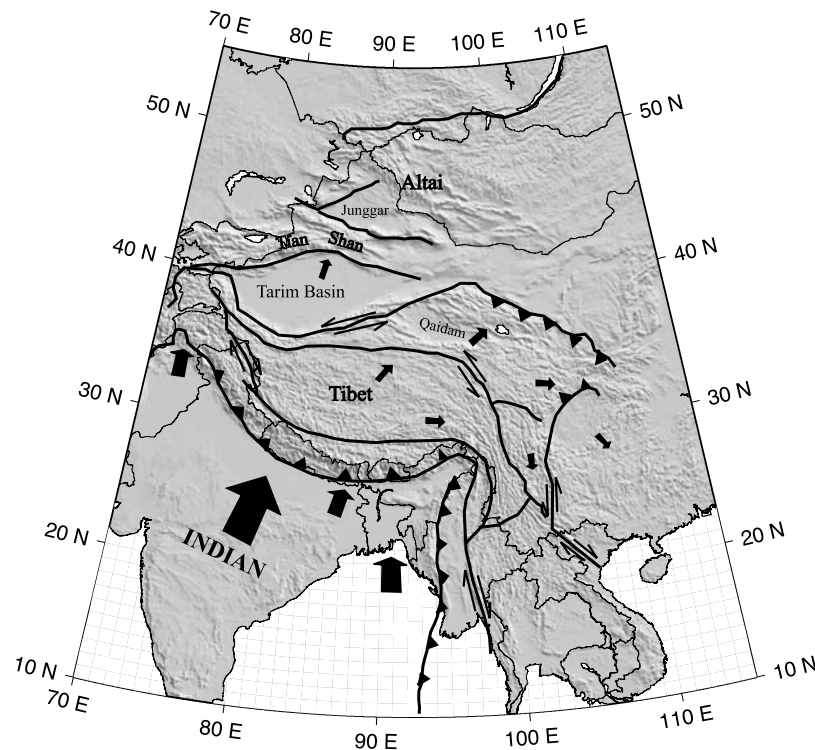


Figure 1. Topographic map of our region of study and surrounding areas. Distribution of major fault zones is indicated with bold lines. Strike-slip faults are represented by half arrows on either side of the fault indicating the sense of slip. Thrust faults are represented by thick lines decorated with triangular teeth pointing to the overriding plate. Large arrows show the average motion of the Indian plate. Small arrows indicate local motion [after *Qin et al.*, 2002]. Reprinted with permission from Elsevier.

other and correlate with known geologic and tectonic features. Using shorter-period surface waves improves the resolution of the shear velocity structure of the crust, but shorter-period surface waves are usually difficult to observe and measure.

[4] The most successful seismic discriminant between explosions and shallow earthquakes is based on differences between the two magnitudes m_b and M_s [Stevens and Day, 1985], which are determined from amplitudes of P waves and Rayleigh waves, respectively. Currently, 20 s period Rayleigh waves are used for teleseismic $m_b - M_s$ discriminants. However, for small magnitude ($m_b < 4$) disturbances recorded at regional distances, 20 s period surface waves are not typically observed. Taylor *et al.* [1989] showed the apparent inability to obtain M_s measurements below $m_b \sim 4$ for the explosions. However, the earthquakes are recorded at lower magnitudes and this suggests the use of negative evidence discriminants for ruling out explosions [e.g., Anderson *et al.*, 1999], but in order to lower the M_s detection threshold, it is necessary to exploit surface waves with periods shorter than 20 s and to enhance the shorter-period surface wave signal requires accurate group velocity maps at shorter periods.

[5] In order to obtain high-resolution dispersion maps and to reduce detection thresholds in the region to discriminate explosions and earthquakes at lower magnitudes, we study the dispersion characteristics of fundamental Rayleigh waves propagating across a small region of central Asia. We focus on developing high-resolution, half a degree cell

size slowness tomography maps from 6 to 30 s period using a Bayesian tomography method [Tarantola, 1987]. The Bayesian framework allows us to integrate large-scale and high-resolution tomographic models from other studies as prior background models and to insure that the new regional model blends into these prior background models. In this paper, we briefly summarize the main geological and tectonic features of the area under study. We follow with a discussion of the data used and the method of measurement employed to produce the group velocity dispersion curves. We then introduce the Bayesian approach to tomography and present a sampling of the computed slowness maps, followed by a brief discussion. We then describe our efforts to validate our refined models with independent data and compare these results with previous studies in the region. We show that we are obtaining high-resolution images that closely mimic geological features in the region.

2. Tectonic Setting

[6] Central Eurasia is an amalgamation of continental blocks that began forming in the early Paleozoic [Zonenshain *et al.*, 1990; Segnör, 1984, 1987] (Figure 1). One of the main events in its evolutionary history is the collision of the Indian subcontinent into Eurasia, which began 50–70 Myr ago [Molnar and Tapponnier, 1975]. The collision has resulted in the uplift of the Himalayan front and the Tibetan Plateau, the reactivation of the Tian Shan orogen, and affected regions as far north as the Baikal

rift [Molnar and Tapponnier, 1975; Yin and Harrison, 2000]. The area has been the subject of numerous studies since it presents an important framework for the understanding of the formation and evolution of continents.

[7] Our study area is located between 69° and 108°E longitude and 29° and 54°N latitude, containing only continental areas. Three of the biggest sedimentary basins in China are within this study region: the Tarim, Junggar, and Qaidam basins. The largest, the Tarim, is 560,000 km² in extent, located between the Tian Shan to the north, the western Kunlun Shan and the Altyn Tagh Shan to the south and southeast, and the Pamir to the west (Figure 1). It has a complicated history of deformation [see Tian *et al.*, 1989]. Archean and Proterozoic rocks form the deeply buried basement, and the sedimentary cover ranges from 17 km within major depression centers to 5 km in the central uplift. The Junggar basin, triangular in shape, is located to the northeast of the Tarim, between the Altay Shan to the north, the Tian Shan to the south, and the Western Junggar mountains to the northwest (Figure 1). Its extent is 130,000 km² and it is underlain by a sedimentary sequence more than 11 km thick [Patton *et al.*, 1985; Chen and Qin, 1989]. The Qaidam basin has an area of 120,000 km² and it is located near the northern edge of the Tibetan Plateau, bounded by the Altyn and Qilian mountains on the north and the Kunlun in the south (Figure 1). The sedimentary thickness has been estimated to range from 8 to 15 km [Gu and Di, 1989].

[8] Besides the natural interest of the oil and gas industries in these basins, the study of their crust and upper mantle structures is of great importance for understanding collisional orogenesis. Most of the tectonic studies across Asia have been focused on the Tibetan Plateau and other mountain belts. However, intermountain basins across central Asia such as the Tarim Basin has played an important role in the evolution of Eurasia, behaving as secondary “indenter” transmitting collisional stresses to the northern mountain ranges [e.g., Molnar and Tapponnier, 1975; Neil and Houseman, 1997]. The fact that Asia is an active continent that possesses a significant intracontinental seismicity, together with the good broadband station coverage across most of Eurasia make surface wave tomography a powerful seismological tool to image the crust and upper mantle structures in the region. In this paper our focus is on obtaining high-resolution tomographic images in the region using shorter-period surface waves and investigating the implications of the models for seismic discrimination.

3. Observations

[9] The region for the data collection was limited to the area enclosed by 35°N to 50°N latitude and 70°E to 95°E longitude. The larger extent of the final region of study was chosen to avoid border effects on the tomography inversion. We used the U.S. Geological Survey (USGS) Preliminary Determination of Epicenters (PDE) catalog to guide the collection of waveform data archived at the Incorporated Research Institutions for Seismology (IRIS) Data Management Center (DMC). For the computation of the group velocity curves, we used the earthquake locations from the National Earthquake Information Center (NEIC) reports. We retrieved broadband waveform data from more than

1,100 events that occurred in the area between January 1997 and May 2002. No magnitude constraints were imposed to improve the dispersion measurement at short periods, but the event depth is constrained between the surface and 100 km depth. Waveforms were obtained from 4 different networks (IRIS/USGS, IRIS/IDA, Chinese Digital Seismic Network, and Geoscope) comprising 11 individual broadband, digital seismic stations (AAK, BRVK, KURK, LSA, LZH, MAKZ, NIL, TLY, ULN, WMQ, WUS) (Figure 2). We were unable to obtain waveforms from two of the stations, GAR (Garm, Tajikistan) and NVS (Novosibirsk, Russia), since they were no longer in operation in the time period of our chosen events.

4. Surface Wave Dispersion Measurements

[10] Measuring the dispersion characteristics of the surface wave signals involves several steps. During preprocessing, to avoid background seismic noise (microseisms or body waves arriving at the same time as surface waves), we inspected the raw seismograms for all events considered. We performed a visual check of the quality of the waveform data to insure reasonable signal-to-noise ratios and to eliminate erroneous recordings. For the reliable waveforms, the instrument response was removed, and the seismograms were decimated to 1 sample/s.

[11] Asia is structurally complex which not only makes interpretation in terms of structural models difficult, but also complicates the waveforms on which the measurement method is applied. This is especially true on regional seismograms at shorter periods. For example, in areas of large velocity contrasts such as the area around the Tarim basin, and particularly for near-grazing incidence paths and at high frequencies, the Rayleigh waves would split into two waves (one traveling around the basin and another passing through it), causing multiple surface wave arrivals [Stevens *et al.*, 2004]. We did not consider in our study suspicious dispersion curves that showed some evidence of this problem during the measurement. We applied a multiple-filter analysis of the seismograms [Dziewonski *et al.*, 1969; Herrmann, 1973] to estimate the surface wave group velocities. A narrow-band Gaussian filter with peak amplitude centered at the desired period is applied to the original seismogram in the frequency domain. The peak of the envelope of the corresponding time domain signal is used as an estimate of the group delay time. Assuming that the wave followed the great circle arc between the source and the receiver, the group velocity for a given period is estimated by dividing the epicentral distance by the group arrival time. The process is repeated for each period of interest and is plotted versus group velocity.

[12] Once group velocities have been estimated, a mode isolation filter [Herrin and Goforth, 1977] can be constructed and applied to the signal to isolate the fundamental mode. This phase match filtering technique provides smooth and stable spectral amplitudes, so the final results are less contaminated by higher modes and multipathing arrivals simplifying the estimation of signal phase. Figure 3 shows an example of the group velocity estimation procedure for Rayleigh waves. A contour diagram of the seismogram envelope is displayed where the Rayleigh wave group velocity estimates are identified by red diamonds, the

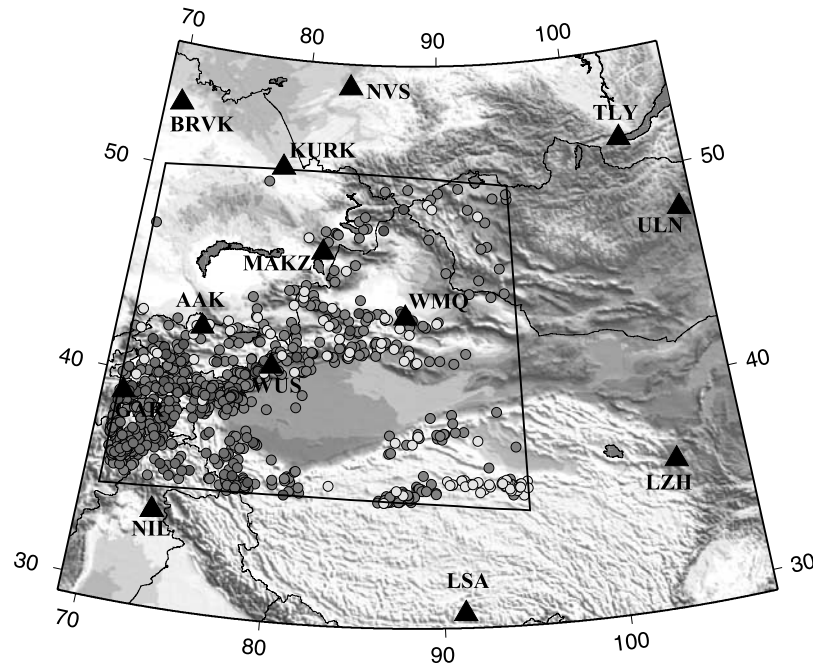


Figure 2. Topographic map of the region of central Asia under study. The black box encloses the data collection area. Events are shown as circles of different colors depending of the event depth: yellow for depths up to 30 km, red from 30 to 60 km, blue for deeper events (up to 100 km), and gray when depth is 33 km, which means that it is unknown. Stations used are shown as black triangles. See color version of this figure at back of this issue.

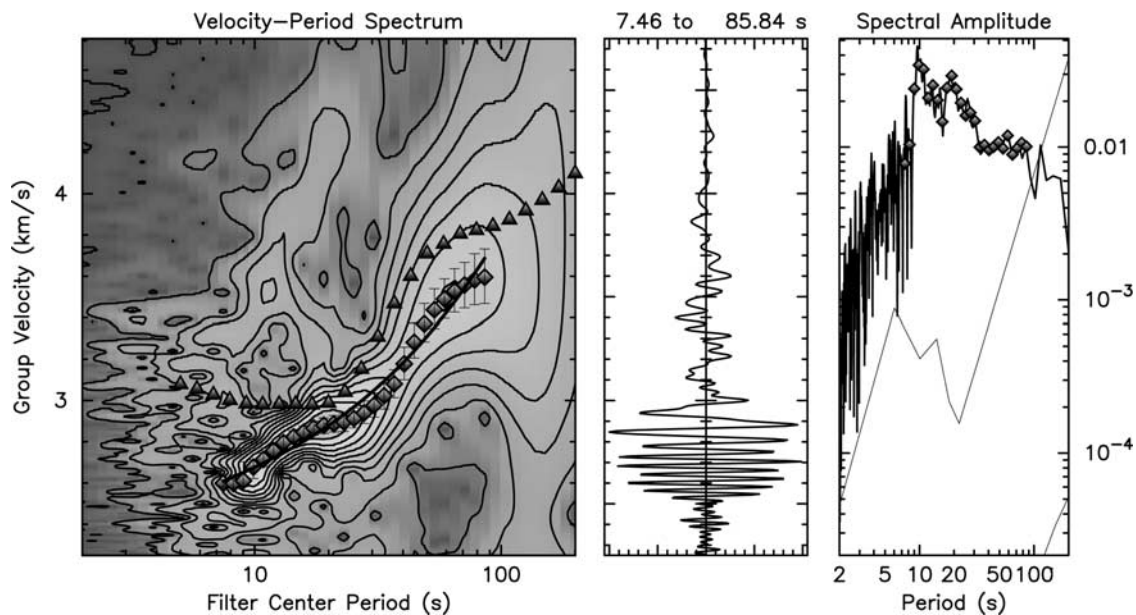


Figure 3. Display illustrating the method used to measure group velocities from an earthquake (2 May 1995, 1148:00 UT) recorded 1665.7 km far away, with an azimuth of 51.5, at station TLY, Talaya, Russia. (left) A contour diagram of the seismogram envelope. Warm colors indicate bigger amplitudes, and cold colors represent smaller amplitudes. The Rayleigh wave group velocity points are identified by red diamonds, the spline fit of the group velocities is depicted by the blue line, and the reference curve, which in this case is Jih's [1998] China crustal model, is plotted as black triangles. (middle) The seismogram is displayed along the group velocity axis. (right) The amplitude spectrum and the sample points along with the USGS low- and high-noise curves. See color version of this figure at back of this issue.

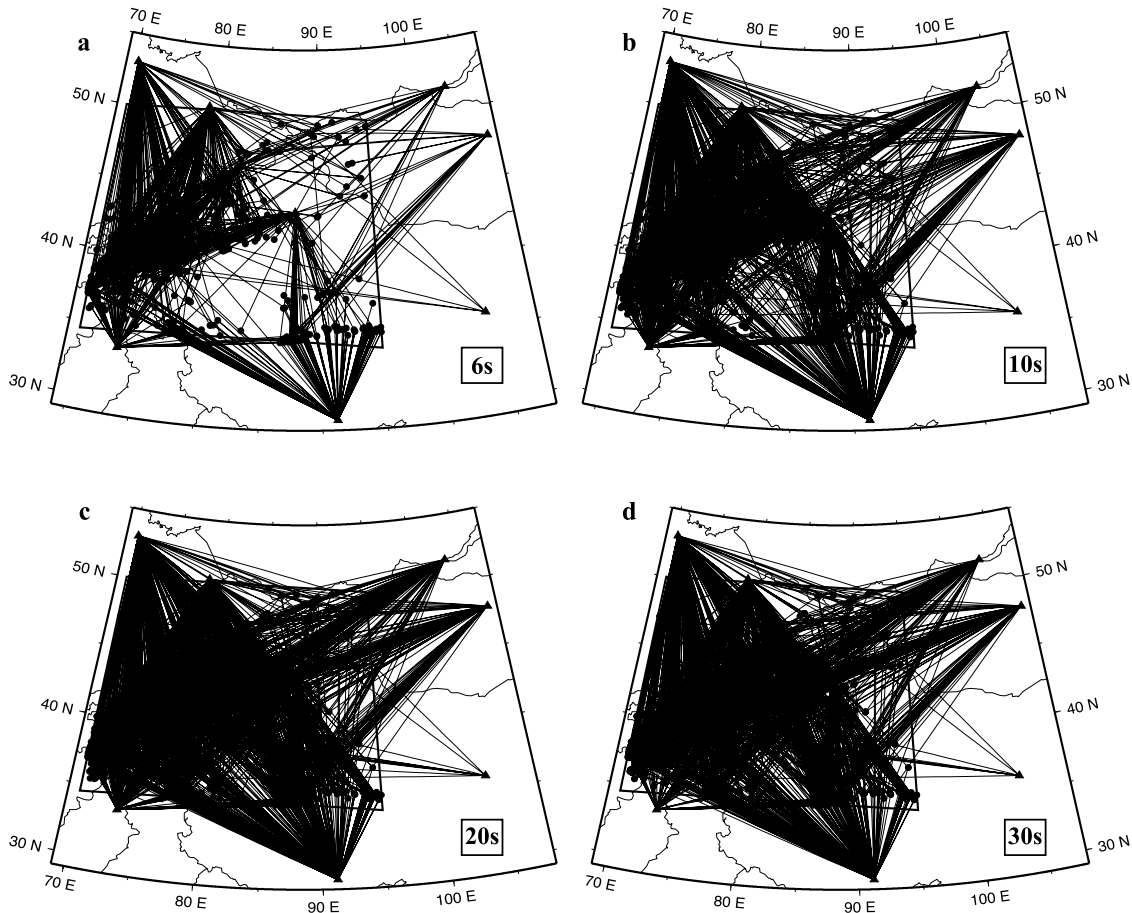


Figure 4. Maps of the region under study showing Rayleigh wave great circle ray paths representing the data used in the tomographic inversions at (a) $T = 6$ s, (b) $T = 10$ s, (c) $T = 20$ s, and (d) $T = 30$ s.

spline fit to the measurements by the blue line, and the black triangles are a reference curve, which in this case is *Jih's* [1998] China crustal model. The reference curve serves as a guide for picking a stable frequency window, but it is not used in our inversion. We window the group velocity measurements by choosing a period range where the curves are continuous. The seismogram is also displayed along the group velocity axis, and the amplitude spectrum and the sample points are shown along with the USGS low- and high-noise curves [Peterson, 1993].

[13] Unfortunately, because of some of the moderate earthquake magnitudes and short path lengths, reliable group velocity measurements could not be obtained for every single event station pair and at the desired period range. Therefore the final path coverage is not uniform for all the periods and the lower the period of interest, the less dense the ray path coverage. Figure 4 shows the ray path coverage at four different periods (6, 10, 20, and 30 s). The path numbers start decreasing for periods over 25 s. In this study we are interested in the short-period range (up to 30 s), but our dispersion measurements extend up to over 100 s. We focus on the measurements from 6 to 30 s.

5. Bayesian Tomography

[14] We used the Rayleigh wave group velocity dispersion curves to compute slowness tomography maps for

individual periods. We divided our region of study into a $0.5^\circ \times 0.5^\circ$ grid of constant slownesses. Our goal is to find the slowness model consistent with the measured travel time (group delay) data. Let \mathbf{d} be the measured travel time m vector such $\mathbf{d} = (d_1, d_2, \dots, d_m)$ where d_i is the travel time along the i th ray path. Then \mathbf{m} is the model slowness n vector $\mathbf{m} = (m_1, m_2, \dots, m_n)$ with m_j being the slowness of the j th cell, satisfying

$$\mathbf{d} = \mathbf{G}\mathbf{m} \quad (1)$$

where \mathbf{G} is an $m \times n$ matrix whose elements l_{ij} are determined by the i th ray path through the j th cell of the model. We assume a first-order path, the great circle.

[15] The inversion problem is reduced to solving the system of linear equations in (1). For that we used a Bayesian approach [Tarantola, 1987; Taylor et al., 2003]

$$P_L(\mathbf{d}, \mathbf{m}) = P_G(\mathbf{d}|\mathbf{m})P_P(\mathbf{d}, \mathbf{m}) \quad (2)$$

where $P_G(\mathbf{d}|\mathbf{m})$ is the conditional probability of the data given the model parameters in (1), $P_P(\mathbf{d}, \mathbf{m})$ is the prior joint probability distribution of the data and the prior model parameters, and $P_L(\mathbf{d}, \mathbf{m})$ is the joint posterior probability distribution used to find the maximum likelihood point given the most probable combination of predicted data and

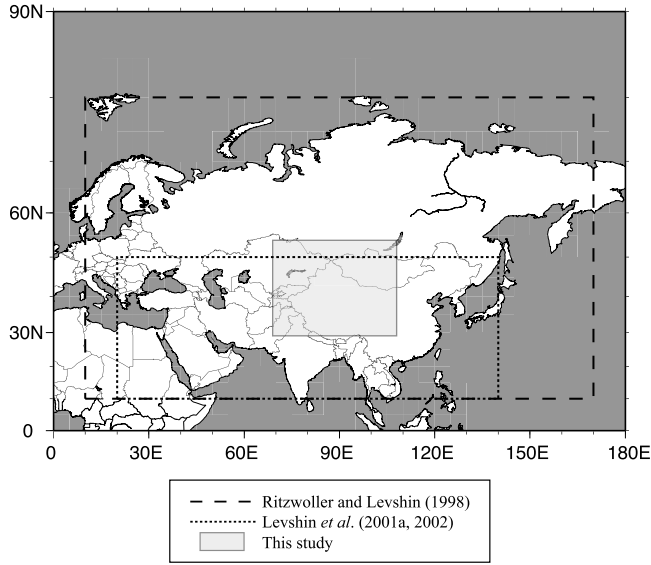


Figure 5. Geographic coverage of the different group velocity maps used in constructing our a priori map. Note that *Stevens et al.*'s [2001] maps are global. Also shown in a light gray box is the region under study.

model parameters. Assuming independence of the input data and the prior model parameters

$$P_P(\mathbf{d}, \mathbf{m}) = P_P(\mathbf{d})P_P(\mathbf{m}) \quad (3)$$

[16] The solution to (1) is given by the marginal distribution of $P_L(\mathbf{d}, \mathbf{m})$

$$P_L(\mathbf{d}, \mathbf{m}) = \int_D P_L(\mathbf{d}, \mathbf{m}) d\mathbf{d} = P_P(\mathbf{m}) \int_D P_P(\mathbf{d}) P_G(\mathbf{d}|\mathbf{m}) d\mathbf{d} \quad (4)$$

[17] For the general linear Gaussian case (least squares), the solution to equation (1) is given by [Tarantola, 1987]

$$\langle \mathbf{m} \rangle = \mathbf{m}_p + [\mathbf{G}^T \mathbf{C}_d^{-1} \mathbf{G} + \mathbf{C}_m^{-1}]^{-1} \mathbf{G}^T \mathbf{C}_d^{-1} (\mathbf{d} - \mathbf{G} \mathbf{m}_p) \quad (5)$$

where the brackets indicate that we are dealing with a mean value and \mathbf{m}_p is the a priori model, \mathbf{C}_d is the data covariance matrix, and \mathbf{C}_m is the covariance of the a priori model. The superscript T means transpose, and the superscript -1 means inverse. Although we are experimenting with full covariance matrices for the data and the model parameters as a way to decluster the events and to smooth the final models, for now the data and model parameters are considered independent and their covariance matrices are assumed to be diagonal.

$$(\mathbf{C}_d)_{ij} = (\sigma_d^2)_{ij} \delta_{ij} \quad (6)$$

$$(\mathbf{C}_m)_{ij} = (\sigma_m^2)_{ij} \delta_{ij} \quad (7)$$

As mentioned before, one of the advantages of using a Bayesian framework is that statistical characteristics of the

data and the a priori information are utilized in the inversion to constrain the results and also their uncertainties [Tarantola, 1987]. When using Gaussian models, the posterior model \mathbf{C}_M and the data \mathbf{C}_D uncertainties are given by

$$\mathbf{C}_M = [\mathbf{G}^T \mathbf{C}_d^{-1} \mathbf{G} + \mathbf{C}_m^{-1}]^{-1} \quad (8)$$

$$\mathbf{C}_D = \mathbf{G} \mathbf{C}_M \mathbf{G}^T \quad (9)$$

and the resolution matrix is given by

$$\mathbf{R} = \mathbf{I} - \mathbf{C}_M \mathbf{C}_m^{-1} \quad (10)$$

Where there is no data, we shouldn't have resolution. From equation (8) it can be seen that where there is no ray coverage, the posterior model uncertainty is approximately equal to the prior model uncertainty (i.e., $\mathbf{C}_M \approx \mathbf{C}_m$), and from equation (10) that implies that $\mathbf{R} \approx 0$ in regions without data.

5.1. The a Priori Model

[18] One of the advantages of using a Bayesian approach is that large-scale and well-accepted tomographic models from previous studies can be used as an a priori background model. However, we could not find a single group velocity model in the literature that would cover our entire region of study for the entire bandwidth of interest. We integrated group velocity maps from different research groups to construct a composite a priori model for our area. *Ritzwoller and Levshin* [1998] computed the group velocity maps of Rayleigh waves from 20 to 200 s for the Eurasia continent. *Levshin et al.* [2001a, 2002] obtained Rayleigh wave group velocity dispersion measurements between 7 and 20 s period and inverted them to obtained tomographic models for the region confined between 10° to 50°N and 20° to 140°E. *Stevens et al.* [2001] calculated global group velocity maps for a period range from 4 s up to 400 s from their global crust and upper mantle structure model. These maps were evaluated [Yang et al., 2002] and proved to be suitable to construct an a priori model for the region of interest.

[19] Restricted by the individual frequencies that the mentioned studies cover, we constructed our composite prior model for periods of 6, 8, 10, 12, 15, 18, 20, 25, and 30 s for this study (longer periods were also considered and computed but those maps are not the focus of this paper and will be reported elsewhere). Figure 5 illustrates the coverage of the maps used in constructing the composite a priori model, together with our region of interest. We used the model provided by *Stevens et al.* [2001] for the 6 s composite map, and the models by *Ritzwoller and Levshin* [1998] were used for periods of 25 and 30 s. For the remaining periods (8 to 20 s), we used the maps from *Levshin et al.* [2001a, 2002] for the region south of 50°N, meanwhile for the north portion, between 50° and 54°N, the *Stevens et al.* [2001] model was integrated except for the period of 20 s that we used the *Ritzwoller and Levshin* [1998] map to fill in that uncovered northernmost portion. The resulting group velocity composite map has one-degree

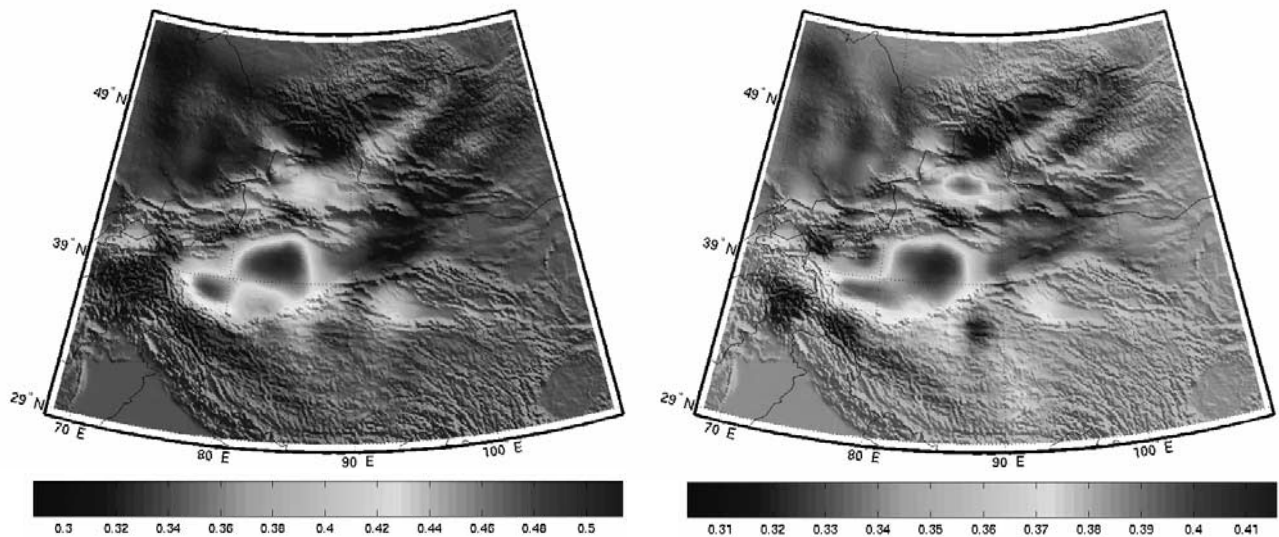


Figure 6. Rayleigh wave slowness maps computed without background model for periods of (left) 10 s and (right) 20 s. The slowness values are s/km. Note the different color scale for each map. See color version of this figure at back of this issue.

cell size and it is consistent with the main tectonic features of the region.

5.2. Event Declustering

[20] Many tomographic studies often do not explicitly include any penalty for event clusters. Our data set exhibits considerable source region redundancy (Figure 4) which could bias the inversion results, i.e., cluster of events following the same path to the same stations would produce an “overweight” of that path in the inversion scheme. This is often manifested as a pronounced “streaking” between event clusters and particular stations in tomographic maps. Giving no weight to the clustered measurements has drawbacks. It is not possible to identify the measurements that we should keep and those that should be discarded; every single measurement provides useful information. Furthermore, taking the average of the measurements in a cluster could significantly change the matrix \mathbf{G} in equation (1). Event mislocations may also have an effect on the estimation of the tomographic maps. If we substitute event clusters by the average, we would be introducing additional source of uncertainty as we choose an epicenter location for that average path. Therefore, instead of taking the approach of averaging the measurements in a cluster, we retain all the dispersion measurements but we moderate their influence by using the cell declustering method described by *Isaaks and Srivastava* [1989].

[21] The cell declustering method uses a moving window to calculate how many measurements fall within particular regions or cells. Each measurement receives a weight that is inversely proportional to the number of events that fall within the same cell. In this way, clustered events will be downweighted because the cells in which they are located will contain several other events. In our case, this weighting factor is incorporated in the data covariance matrix \mathbf{C}_d . Therefore the data covariance matrix, which represents the data weighting,

has two contributions or subweights: the error in the travel time data (obtained from the dispersion measurement error by propagation of errors to a first order) and the declustering weight factor.

6. Rayleigh Wave Slowness Maps

[22] To quantify the importance and the effect of the a priori information, we first computed our model using a homogeneous background model. We inverted group velocities with periods between 10 and 30 s at 5-s intervals using a conjugate gradient-based least squares inversion. Laplacian smoothness constraints were used to stabilize the inversion. We performed an initial inversion to identify outliers, which were down weighted for the inversion that produced the results shown in Figure 6. The variance reduction from the inversion is about 30%, which we could improve with data weighting and constraint tuning, but that is beyond our goals for these inversions. Here our point is to illustrate the gross resolving power of the data with no a priori model. Figure 6 shows the tomography results in this case for periods of 10 and 20 s as an example. The tomographic slowness values are superimposed on a topographic map to ease the identification of plains and basins from mountains. The color scale used is different for each map to keep the details in each image. The images reproduce, with high fidelity, the location and shape of main tectonic and geological features of the region under study proving the imaging power of our data. Low velocities are associated with sedimentary basins such as the Tarim, the Junggar, and the Qaidam basins; meanwhile high velocities are associated with mountainous features such as the Tian Shan.

[23] Once the imaging resolution of our data set has been confirmed, we computed Rayleigh wave slowness tomography maps using the Bayesian approach with the a priori model described in the previous section. For the present study, these models were obtained at 9 different periods

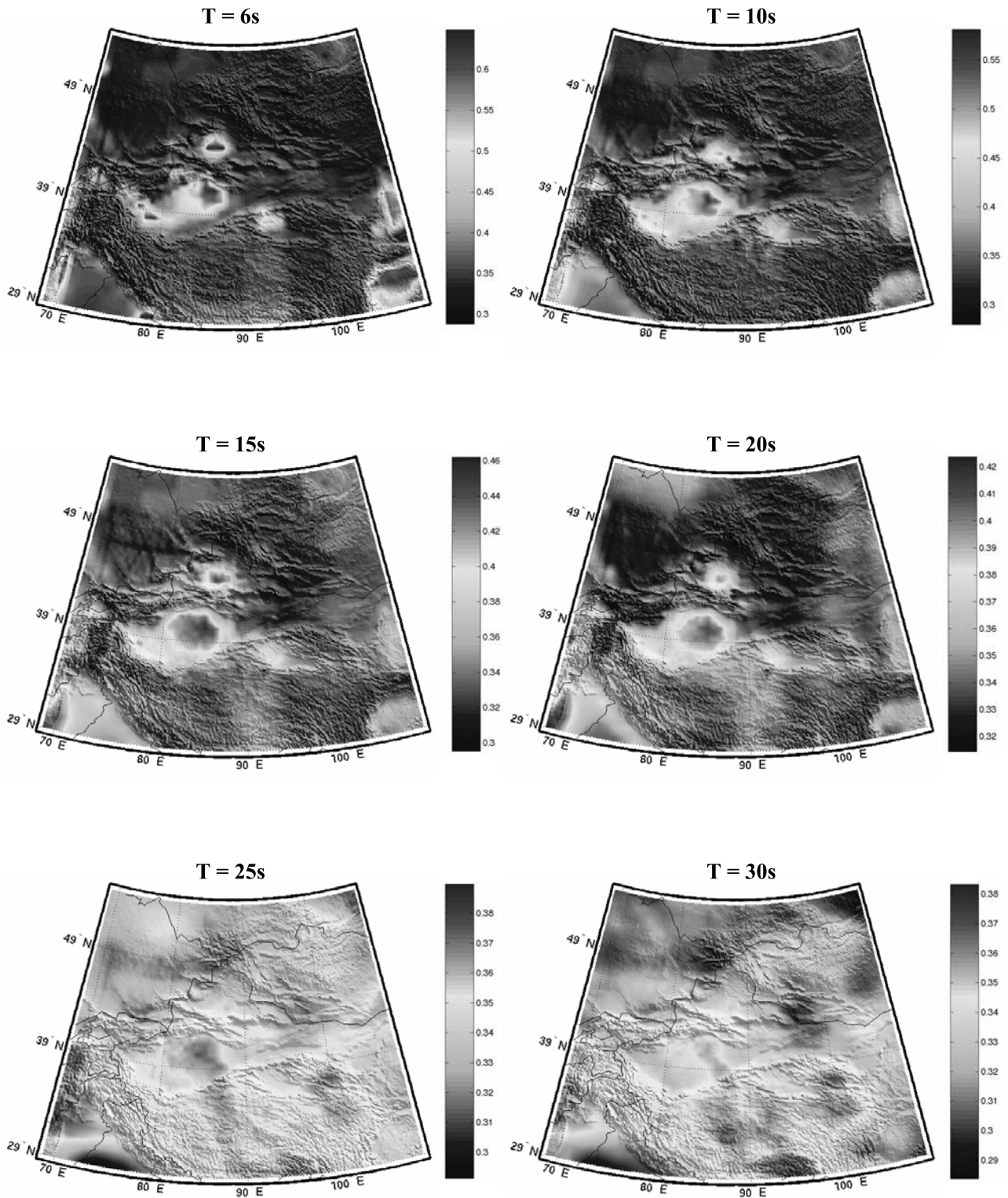


Figure 7. Rayleigh wave slowness maps for different periods. The slowness values are expressed in s/km. Note that the color scale is different for each map. See color version of this figure at back of this issue.

from 6 to 30 s. Figure 7 shows the obtained absolute slowness model at 6, 10, 15, 20, 25, and 30 s. Note that the color scale used is different for each map to keep the details in each image.

[24] The longer the period, the deeper the Rayleigh wave energy penetrates. Thus longer-period Rayleigh waves contain more information about the deep velocity structure, and shorter periods are primarily sensitive to upper crustal

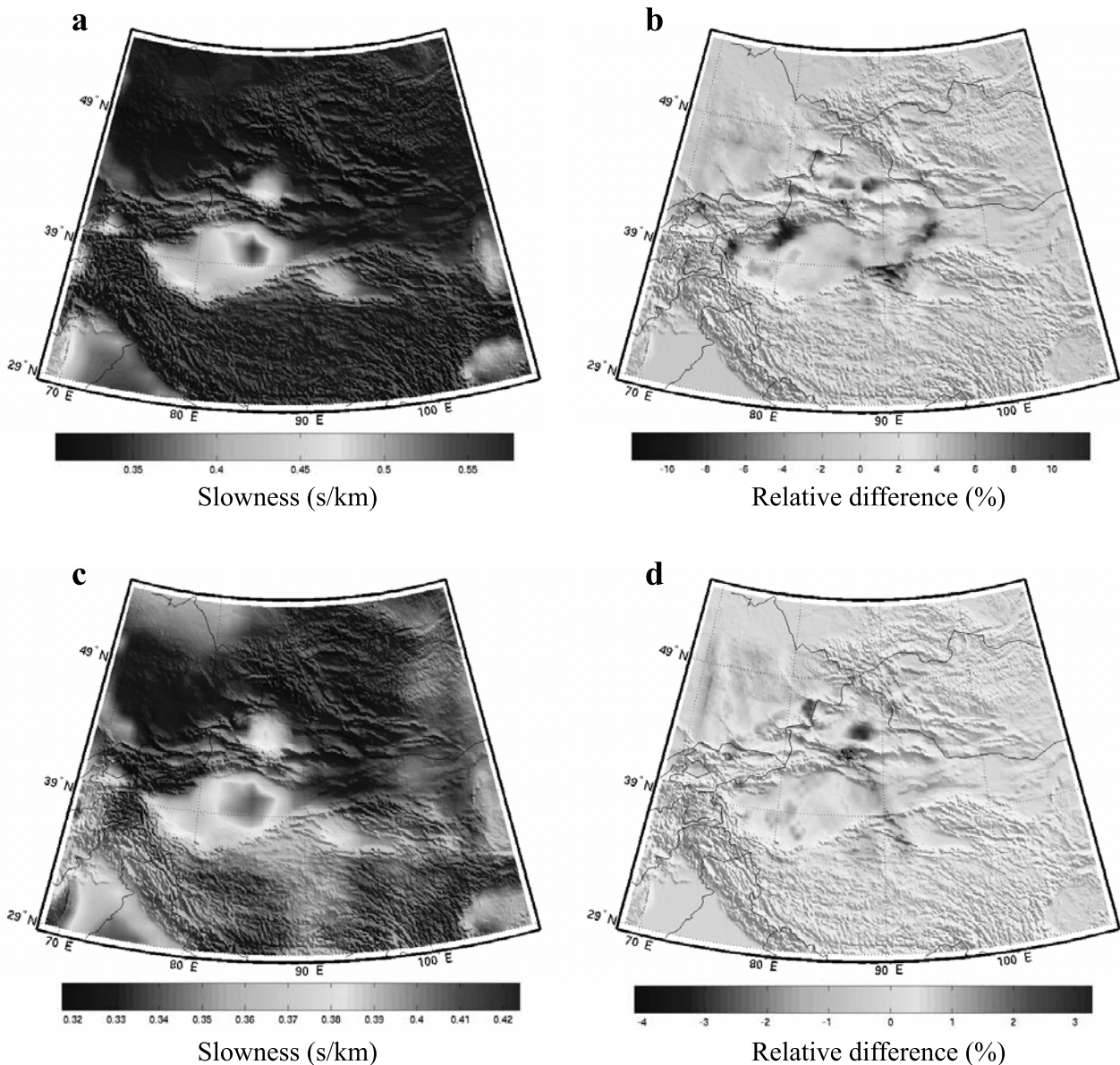


Figure 8. (a) Composite a priori map used for the tomographic inversion at 10 s. (b) Relative difference map between the refined and the reference models at 10 s. (c) Composite a priori map used for the tomographic inversion at 20 s. (d) Relative difference map between the refined and the reference models at 20 s. See color version of this figure at back of this issue.

structures. In general, a good approximation is that surface waves sample to a depth of their wavelength divided by three [Fowler, 1990]. Since we are considering slowness models up to 30 s, we are only focusing in the upper to midcrust.

[25] The tomographic patterns in our model correlate well with known geologic and tectonic features in the area with our shorter-period maps reflecting the shallow crust. Accumulations of relatively young sediments across Eurasia are among the greatest because of the continuing rapid uplift across much of central Asia [Ritzwoller and Levshin, 1998]. The tomographic images display low velocities associated with the known major sedimentary basins, Tarim, Junggar, and Quaidam basins, in the area of central Asia under study. Higher velocities are associated with mountainous tectonic

features such as the Tian Shan. Note that in our image at 6 s period (Figure 7), not the whole Tarim basin shows slow as it would be expected due to the short period of sampling and the thick sediments present in the basin. Analysis suggest that this is a combination of the fact that the a priori model, at 6 s period, shows a similar velocity distribution in the basin, and that our ray path coverage in the area at 6 s is not sufficient (Figure 4). However, we do not discard the possibility of this being related to the great circle path approximation when there is a deep low-velocity zone. Ritzwoller *et al.* [2002] studied the significant differences in surface wave tomography between using geometrical ray theory and scattering theory. They found the greatest differences between the two methods at long periods for long paths but also found differences at short periods and for

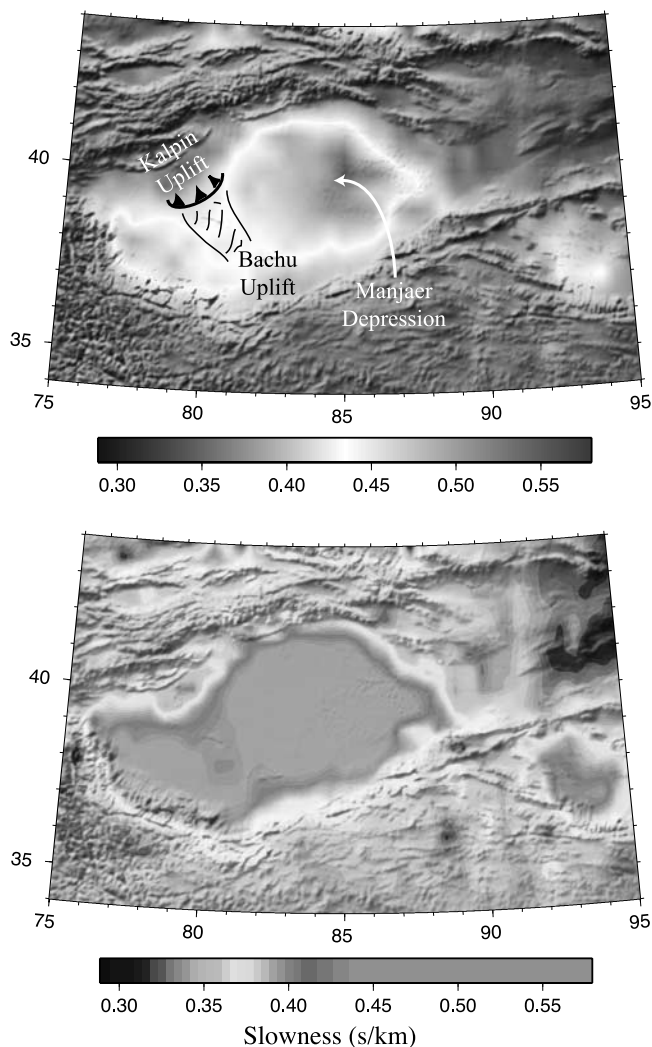


Figure 9. (top) Computed slowness model at 10 s period. Some of the main features of the Tarim basin such as the Manjaer depression and the central uplift are obvious in our refined model. (bottom) The same slowness model plotted in a different color scale to show that even some of the Cenozoic sedimentary cover north of the basin is apparent in our model. See color version of this figure at back of this issue.

short wave paths. On average, diffraction tomography produces larger velocity anomalies and also affects the geometrical pattern of the tomographic features. As the period increases, the imprint of the sedimentary layers diminishes but it does not disappear completely. Synthetic tests showed that the influence of very thick (~ 15 km) layers of sediments over a thick crust remains present at longer periods than it would if there was a thin crust. Therefore our slowness maps for periods over 20 s are influenced not only by the thickness of the crust but also by the thick sediments. As an example, the Tibetan Plateau appears as a low-velocity zone in our slowness maps at 25 and 30 s due to its thick crust (Figure 7), but we can still observe the influence of the thick sediments in the basin.

[26] The importance of the imposed information (a priori model) in the Bayesian approach is shown in Figures 8 and 9. Figure 8 shows the composite a priori model (Figures 8a and 8c) used in the tomographic inversion for periods of 10 s (Figures 8a and 8b) and 20 s (Figures 8c and 8d). These maps are very similar to the ones presented in Figure 7 for the corresponding periods. At first glance, it seems that there is no significant difference between the a priori model and our refined model, suggesting that our inversion does not produce significant new information. However, Figure 6 clearly shows the imaging power of our data, and the maps to the right in Figure 8 showing the relative difference between the prior and this study maps, demonstrate that there are significant differences between the a priori information and the final computed model. These differences, shown to be improvements in the next section, are mainly at the shorter end of this study period band, mostly from 6 to 15 s. These shorter periods are the interesting ones for our final goal to extent the surface wave magnitude estimates to shorter periods and smaller events to reduce the present seismic detection threshold. As period increases the differences between the a priori maps and our refined maps become less significant and our tomographic maps are very close to the initial ones (Figure 8d), demonstrating that our observations at those periods do not contain more information than the prior model.

[27] Figure 9 shows the importance of the nature of the prior information. For the most part, our initial maps [Levshin *et al.*, 2001a] are the result of an inversion that used a pretty detailed crustal model as a starting model [Villaseñor *et al.*, 2001]. This fact together with the importance of the a priori information in the Bayesian framework allow us to obtain high-resolution tomographic images of the region that show geological features in the area besides the large basins. In particular, Figure 9 shows two images of our computed slowness map at 10 s (Figure 9 (bottom) was plotted saturating the higher end of a multicolor palette in order to be able to show features outside the basin). Slower velocities correlate with the Manjaer depression where the sedimentary cover, consisting of Proterozoic and Phanerozoic sequences, reaches 17 km depth [Li *et al.*, 1996]. Faster velocities are associated with the Bachu uplift that may be correlated with the tectonic unloading of some sections of the Tian Shan belt since late Miocene [Yang and Liu, 2002]. Even some of the Cenozoic sedimentary cover between pre-Cenozoic rocks north of the basin [Carroll *et al.*, 2001], shows in our slowness model (Figure 9, bottom).

[28] The standard errors on the computed slowness are shown in Figure 10 for the tomographic maps at periods of 10 s (Figure 10, left) and 20 s (Figure 10, right). Resolution maps are similar to these (i.e., smaller error areas are zones of higher resolution). Not unexpectedly, the slowness map for 20 s period has smaller error than the map at 10 s since it has better ray path coverage. Also, the smallest errors for each period are found where the density of crossing ray paths is highest. From equation (8), it can be seen that $C_M \approx C_m$ where there is no ray path coverage, so the posterior model error is approximately equal to the a priori model error outside the region where we collected data.

[29] The fit to the data used for the computation of our slowness model is shown in Figure 11. The residual distributions for the different periods are Gaussian-like with

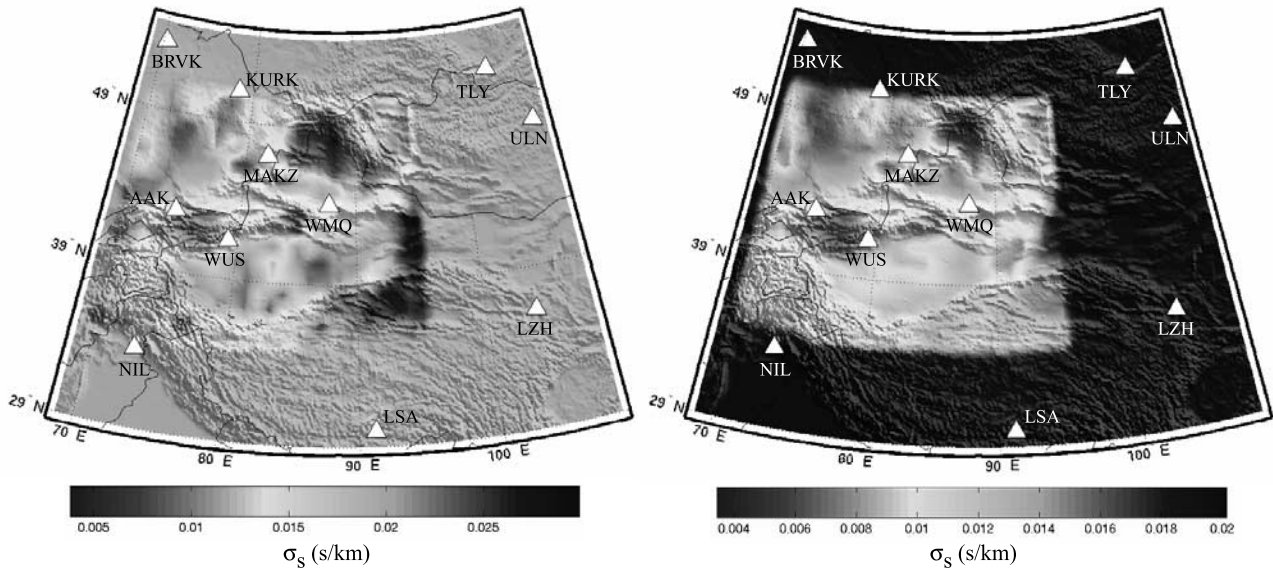


Figure 10. Standard errors on the slowness values for the tomographic model at (left) 10 s and (right) 20 s periods. Stations used are represented by the white triangles. See color version of this figure at back of this issue.

a mean ranging from -0.01 to 0.03 km/s depending on the period, and with standard deviations ranging from 0.15 to 0.19 km/s (Figure 11, top). As expected, residuals increase with group delay (Figure 11, bottom) and we obtained larger residuals for longer paths.

7. Seismic Discrimination Implications

[30] One of the most successful discriminants is based on the differences between the two magnitudes m_b and M_s

[e.g., *Stevens and Day, 1985*], which are determined from amplitudes of P waves and Rayleigh waves, respectively. Accurate slowness maps will facilitate the estimation of M_s near 20 s period. However, for small magnitude ($m_b < 4$) disturbances recorded at regional distances, 20 s period surface waves are not typically observed and/or measured. Because of crustal structure effects, high-amplitude Airy phases (occurring at group velocity minima) at intermediate periods (e.g., 10–14 s) are more commonly observed. Shorter periods ($T < 10$ s) are usually contaminated by

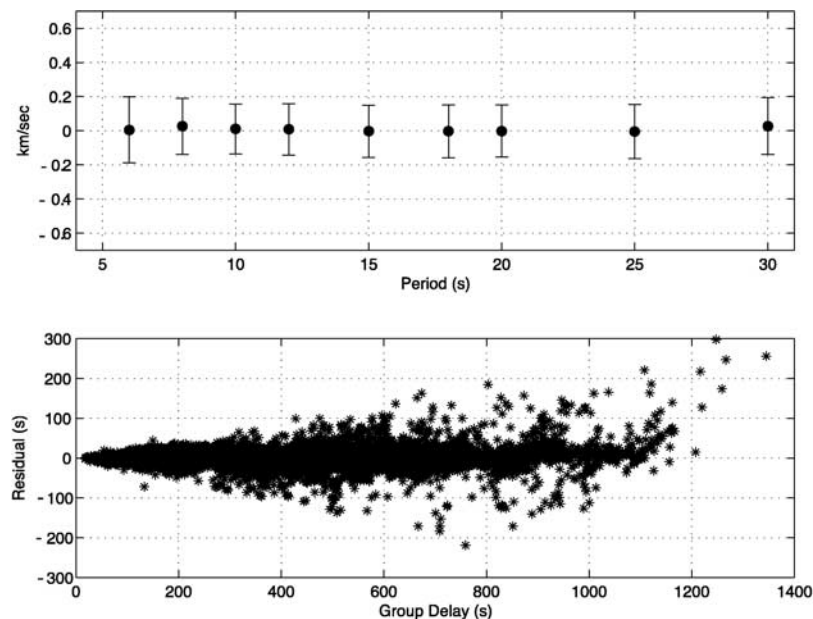


Figure 11. Fit to the data used in the tomographic inversion. (top) Mean of the residual, obtained by subtracting the measurements from the predictions, as a function of period with one standard deviation of the residual as error bars. (bottom) Residual as a function of group delay. Data for all periods are included.

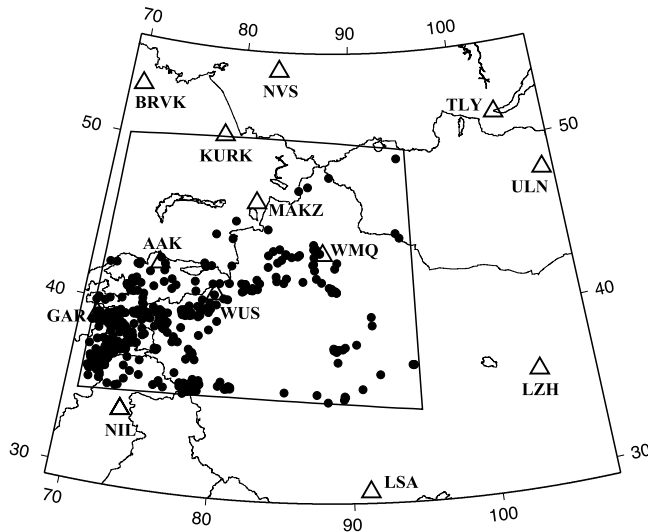


Figure 12. Map of the study region showing the epicenters of the independent events used for the validation of our slowness model. The stations used, shown as open triangles, are the same ones as those in Figure 2.

microseismic noise and are disrupted by heterogeneous near-surface velocity structure. Although intermediate-period surface waves for small regional disturbances have lower detection thresholds than those at 20 s, they are more affected by source depth (making earthquakes appear more

explosion like) and propagation. Thus intermediate-period $m_b - M_s$ discriminants may appear to be more explosion-like for earthquakes occurring below midcrustal depths. Taylor *et al.* [1989] showed the apparent inability to obtain M_s measurements below $m_b \sim 4$ for the explosions. This is because explosions only weakly generate shear waves that contribute to surface waves. However, the earthquakes are recorded at lower magnitudes, and this suggests the use of negative evidence discriminants for ruling out explosions [e.g., Anderson *et al.*, 1999]. If a surface wave can be detected below $m_b \sim 3.5$ it is likely that the event was a shallow earthquake and not an explosion (thus eliminating the need for further analysis). In order to lower the M_s detection threshold, it is necessary to explore surface waves with periods shorter than 20 s. Enhancing the shorter-period surface wave signal requires group velocity maps accurate at shorter periods and for shorter paths.

[31] To test the effectiveness of our model, we assembled independent data that were not used in the computation of the slowness models. We retrieved broadband waveform data from 641 events that occurred in the area ($35^\circ\text{--}50^\circ\text{N}$, $70^\circ\text{--}95^\circ\text{E}$) between January 1993 and December 1996. The digital stations that recorded the events were the same as previously used. Figure 12 is a map of the location of these independent events along with the stations. We measured the dispersion curves along the new event-station pair paths, as described above. The total number of measurements is 8328. As a note, let us mention here that, just for completeness of this study and a posteriori, we actually used these new data for a full inversion of the whole data set (1993–

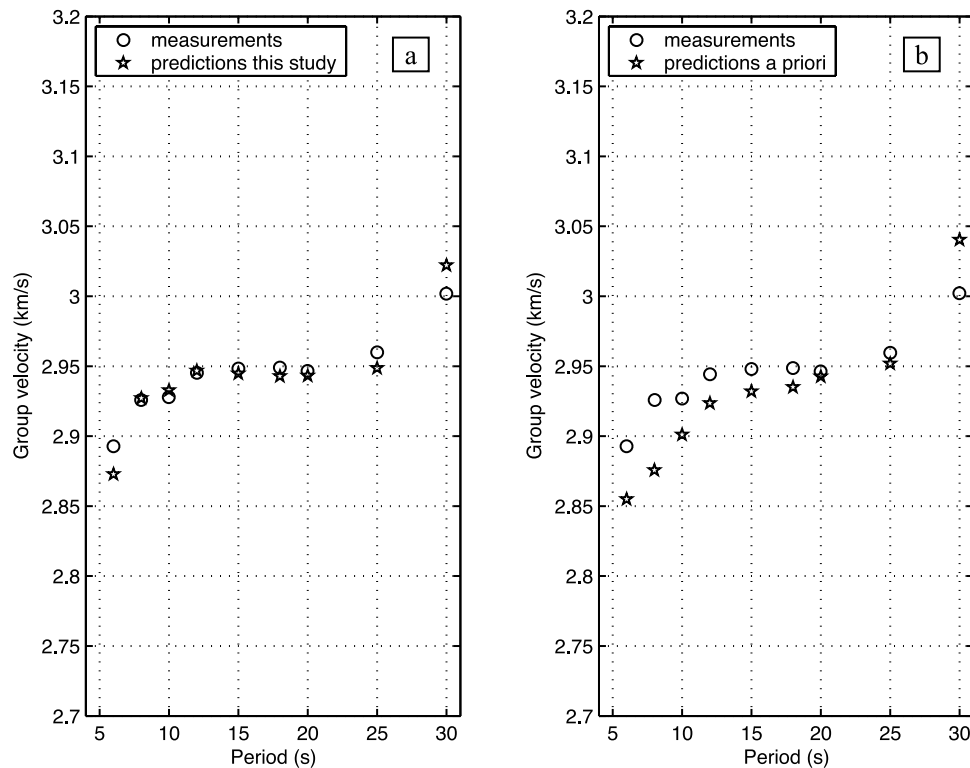


Figure 13. Residual analysis results. (a) Average group velocities from the measurements and our model predictions. (b) Average group velocities from the measurements and the a priori model predictions. Comparison of both plots shows the improvement, especially at shorter periods, obtained by using the refined model.

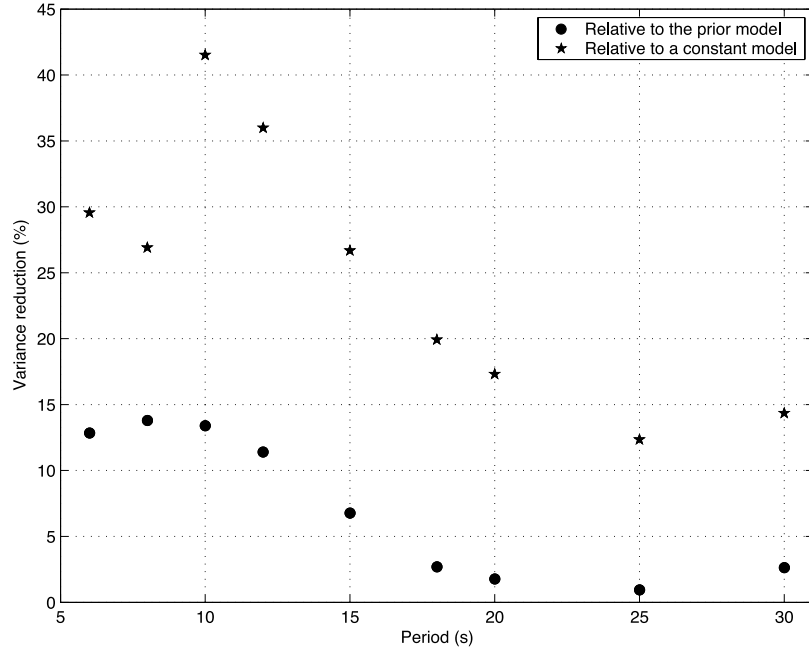


Figure 14. Variance reduction relative to two different velocity models as a function of period. Circles are the variance reduction of our refined slowness model relative to the a priori background composite model used in the Bayesian inversion. Stars are the values of variance reduction relative to a constant model, which is equal to the mean slowness of our refined model for each period.

2002). As it was expected, we found no significant change in the output model because of the similar location distribution of the new events.

[32] To evaluate the performance of our slowness model in predicting the independent measurements, we first calculated the differences between measured and predicted group velocity values and analyzed the residual distribution. Figure 13 shows the results of the residual analysis for our slowness model and for the a priori model. The predictions match the data closely and better than the a priori model. The difference in performance is most obvious at shorter periods (up to 15 s). Residual distributions obtained by subtracting the measurements from our predictions for individual periods are Gaussian-like with a mean close to zero (from -0.02 to $+0.02$ km/s depending on the period) and with standard deviations ranging from 0.18 to 0.23 km/s. Considering all the periods together, the residuals range between -0.5 and $+0.5$ km/s. Also the residual distribution for each individual station is Gaussian-like with a close to zero mean.

[33] We also considered another parameter of misfit as the variance reduction relative to the a priori model for each period of interest. We defined the variance reduction (γ) for each period as

$$\gamma = 1 - \frac{\sum_i (U_i^{\text{pred}} - U_i^{\text{obs}})^2}{\sum_i (U_i^{\text{prior}} - U_i^{\text{obs}})^2} \quad (11)$$

where i is the event-station path index, U_i^{pred} is our model predicted group velocity for path i , U_i^{obs} is the measured group velocity for path i , and U_i^{prior} is the a priori predicted

group velocity for path i . Figure 14 shows the results of the variance reduction calculation. Once again, the improvement is most apparent for the shortest periods, which is desirable for seismic discrimination. The variance reduction values are not that large, but it is not surprising considering that the a priori model is a composite of well-accepted tomographic models for the region. To show overall performance, we also calculated the variance reduction relative to a constant model. This constant model is equal to the mean slowness of our model for each period. The results are also presented in Figure 14 and the achievement of larger variance reduction can be seen.

[34] We further evaluate the performance of our slowness model using a surface wave detection method [Stevens and McLaughlin, 2001] and test for the improvement of our model in detecting surface waves with respect to a 1-D China model [Jih, 1998] and the Preliminary Reference Earth Model (PREM from Dziewonski and Anderson [1981]). The method applies multiple band-pass filters to the data and measures the arrival time of the peak amplitude at each period. If a certain percentage of the measurements fall within the time range predicted by our slowness maps, the method declares a surface wave detection. The equation used to define the arrival time interval for a detection is

$$\frac{\Delta}{v_p + v_o} - p_o T - t_o < t < \frac{\Delta}{v_p - v_o} + p_o T + t_o \quad (12)$$

where Δ is the epicentral distance, v_p is the predicted group velocity, T is the period, and v_o , p_o , and t_o are constants that the user can use to adjust the width of the arrival time interval. We followed Stevens and McLaughlin [2001] and set these constants to 0.2 km/s, 1, and 0 s, respectively. The

surface wave detection is considered successful if 70% of the measurements fall within the time interval defined as above. The number of surface wave detections using group velocity predictions calculated from the Preliminary Reference Earth Model [Dziewonski and Anderson, 1981] is 71. Using Jih's [1998] China crustal model, we obtain 420 detections; meanwhile, using the maps computed in this study, the number of detections is 485. The use of our group velocity maps increased the number of surface wave detections by 15% with respect to using the China model.

8. Conclusions

[35] We have refined previous Rayleigh wave group velocity tomographic maps in central Asia using a Bayesian framework. We analyzed waveform data from more than 1100 events recorded by 11 seismic stations in a small region of central Asia. These recordings produced more than 6500 paths, and we estimated individual dispersion curves for each of them performing a multiple filter analysis together with the application of phase match filter techniques. The inversion of these dispersion curves using a Bayesian approach produced Rayleigh wave slowness tomography maps in the period band between 6 and 30 s. Our refined maps are close to the background model at long periods, but they contain significant additional information at the shorter periods (6–15 s), and the grid size is smaller (0.5° compared to 1° for the a priori model). Additionally, our model shows high resolution and correlates well with the tectonics and geology of the area. In general, the tomographic images display low velocities associated with the known sedimentary basins such as Tarim, Junggar and Qaidam basins. High velocities relate to the mountainous tectonic features such as Tian Shan. We have also evaluated the effectiveness of our model in predicting measured data and show that our images improve seismic discrimination, especially at shorter periods. In particular, improved short-period slowness maps lower the M_s detection thresholds for construction of regional m_b : M_s discriminants, a useful and robust discriminant for nuclear explosion monitoring.

[36] **Acknowledgments.** We thank Anatoli Levshin, Michael Ritzwoller, and Jeffery Stevens for kindly providing the tomographic maps used in this study to construct the a priori model. Special thanks to the Data Management Center of IRIS for making the data accessible to all of us. Thanks to Paul Wessel and Walter Smith for developing and maintaining their Generic Mapping Tool (GMT). We are grateful to H. J. Patton for his valuable help and insight in this study. We thank J. Stevens, M. Ritzwoller, and the editors for their constructive comments and suggestions that help to improve this manuscript. This work was performed under the auspices of the U.S. Department of Energy by Los Alamos National Laboratory under contract W-7405-ENG-36.

References

- Anderson, D. N., S. R. Taylor, and K. K. Anderson (1999), Discrimination information in phase amplitude thresholds with application to western China regional data, *Bull. Seismol. Soc. Am.*, **89**, 648–656.
- Bird, P., and M. N. Tököz (1977), Strong attenuation of Rayleigh waves in Tibet, *Nature*, **266**, 161–163.
- Bourjot, L., and B. Romanowicz (1992), Crust and upper mantle tomography in Tibet using surface waves, *Geophys. Res. Lett.*, **19**, 881–884.
- Brandon, C., and B. Romanowicz (1986), A 'no-lid' zone in the central Chang-Thang platform of Tibet: Evidence from pure path phase velocity measurements of long-period Rayleigh waves, *J. Geophys. Res.*, **91**, 6547–6564.
- Butler, R., et al. (2004), The Global Seismographic Network surpasses its design goal, *Eos Trans. AGU*, **85**, 225, 229.
- Carroll, A. R., S. A. Graham, E. Z. Chang, and C. McKnight (2001), Sinian through Permian tectonostratigraphic evolution of the northwestern Tarim Basin, China, in *Paleozoic and Mesozoic Tectonic Evolution of Central and Eastern Asia: From Continental Assembly to Intracontinental Deformation*, edited by M. S. Hendrix and G. A. Davis, *Mem. Geol. Soc. Am.*, **194**, 47–69.
- Chen, H., and D. Qin (1989), Unstable cratonic and paleozoic basins of China, in *Chinese Sedimentary Basins, Sediment. Basins World*, vol. 1, edited by X. Zhu, pp. 7–16, Elsevier, New York.
- Chen, W. P., and P. Molnar (1975), Short-period Rayleigh wave dispersion across the Tibetan Plateau, *Bull. Seismol. Soc. Am.*, **65**, 1051–1057.
- Curtis, A., and J. H. Woodhouse (1997), Crust and upper mantle shear velocity structure beneath the Tibetan Plateau and surrounding regions from interevent surface wave phase velocity inversion, *J. Geophys. Res.*, **102**, 11,789–11,813.
- Dziewonski, A. M. (1971), On regional differences in dispersion of mantle waves, *Geophys. J. R. Astron. Soc.*, **22**, 289–325.
- Dziewonski, A. M., and D. L. Anderson (1981), Preliminary reference Earth model, *Phys. Earth Planet. Inter.*, **25**, 297–356.
- Dziewonski, A. M., S. Bloch, and M. Landisman (1969), A technique for the analysis of transient seismic signals, *Bull. Seismol. Soc. Am.*, **59**, 427–444.
- Ewing, W. M., W. S. Jardetsky, and F. Press (1957), *Elastic Waves in Layered Media*, McGraw-Hill, New York.
- Feng, C. C., and T. L. Teng (1983), Three-dimensional crust and upper mantle structure of the Eurasian continent, *J. Geophys. Res.*, **88**, 2261–2272.
- Fowler, C. M. R. (1990), *The Solid Earth: An Introduction to Global Geophysics*, Cambridge Univ. Press, New York.
- Godey, S., R. Snieder, A. Villaseñor, and H. M. Benz (2003), Surface wave tomography of North America and the Caribbean using global and regional broadband networks: Phase velocity maps and limitations of ray theory, *Geophys. J. Int.*, **152**, 620–632.
- Gu, S. S., and H. S. Di (1989), Mechanism of formation of the Qaidam basin and its control on petroleum, in *Chinese Sedimentary Basins, Sediment. Basins World*, vol. 1, edited by X. Zhu, pp. 45–51, Elsevier, New York.
- Herrin, E., and T. Goforth (1977), Phase matched filters: Application to the study of Rayleigh waves, *Bull. Seismol. Soc. Am.*, **67**, 1259–1275.
- Herrmann, R. B. (1973), Some aspects of band-pass filtering of surface waves, *Bull. Seismol. Soc. Am.*, **63**, 663–671.
- Huang, Z., W. Su, Y. Peng, Y. Zheng, and H. Li (2003), Rayleigh wave tomography of China and adjacent regions, *J. Geophys. Res.*, **108**(B2), 2073, doi:10.1029/2001JB001696.
- Isaaks, E. H., and R. M. Srivastava (1989), *An Introduction to Applied Geostatistics*, 561 pp., Oxford Univ. Press, New York.
- Jih, R. S. (1998), Location calibration efforts in China, paper presented at the 20th Annual Seismic Research Symposium on Monitoring a Comprehensive Test Ban Treaty, U.S. Dep. of Energy, Santa Fe, N. M.
- Jobert, N., B. Jourmet, G. Jobert, A. Him, and S. K. Zhong (1985), Deep structure of southern Tibet inferred from the dispersion of Rayleigh waves through a long-period seismic network, *Nature*, **313**, 386–388.
- Knopoff, L. (1972), Observation and inversion of surface wave dispersion, *Tectonophysics*, **13**, 497–519.
- Levshin, A. L., and M. H. Ritzwoller (1995), Characteristics of surface waves generated by events on and near the Chinese nuclear test site, *Geophys. J. Int.*, **123**, 131–149.
- Levshin, A. L., L. I. Ratnikova, and J. Berger (1992), Peculiarities of surface wave propagation across central Eurasia, *Bull. Seismol. Soc. Am.*, **82**, 2464–2493.
- Levshin, A. L., M. H. Ritzwoller, and L. I. Ratnikova (1994), The nature and cause of polarization anomalies of surface waves crossing northern and central Eurasia, *Geophys. J. Int.*, **117**, 577–590.
- Levshin, A. L., M. H. Ritzwoller, M. P. Barmin, and J. L. Stevens (2001a), Short period group velocity measurements and maps in central Asia, paper presented at the 23rd Seismic Research Review: Worldwide Monitoring of Nuclear Explosions, Natl. Nucl. Secur. Admin., Jackson Hole, Wyo.
- Levshin, A. L., M. H. Ritzwoller, M. P. Barmin, A. Villaseñor, and C. A. Padgett (2001b), New constraints on the arctic crust and uppermost mantle: Surface wave group velocities, P_n , and S_n , *Phys. Earth Planet. Inter.*, **123**, 185–204.
- Levshin, A. L., J. L. Stevens, M. H. Ritzwoller, and D. A. Adams (2002), Short-period (7-s to 15-s) group velocity measurements and maps in central Asia, paper presented at the 24th Seismic Research Review—Nuclear Explosion Monitoring: Innovation and Integration, Natl. Nucl. Secur. Admin., Ponte Vedra Beach, Fla.
- Li, D., D. Liang, C. Jia, G. Wang, Q. Wu, and D. He (1996), Hydrocarbon accumulations in the Tarim Basin, China, *AAPG Bull.*, **80**, 1587–1603.

- Molnar, P., and P. Tapponnier (1975), Cenozoic tectonics of Asia: Effects of a continental collision, *Science*, **189**, 419–426.
- Neil, E., and G. Houseman (1997), Geodynamics of the Tarim Basin and the Tian Shan in central Asia, *Tectonics*, **16**, 571–584.
- Oliver, J. (1962), A summary of observed surface wave dispersion, *Bull. Seismol. Soc. Am.*, **52**, 81–86.
- Patton, H. (1980), Crustal and upper mantle structure of the Eurasian continent from the phase velocity and Q of surface waves, *Rev. Geophys.*, **18**, 605–625.
- Patton, H. J., S. R. Taylor, D. B. Harris, and J. M. Mills (1985), The utility of regional Chinese seismograms for source and path studies in central Asia, *Geophys. J. R. Astron. Soc.*, **81**, 469–478.
- Peterson, J. R. (1993), Observations and modeling of seismic background noise, *U.S. Geol. Surv. Open File Rep.*, 93-322, 94 pp.
- Pines, I., T. L. Teng, and R. Rosenthal (1980), A surface wave dispersion study of the crustal and upper mantle structure of China, *J. Geophys. Res.*, **85**, 3829–3844.
- Qin, C., C. Papazachos, and E. Papadimitriou (2002), Velocity field for crustal deformation in China derived from seismic moment tensor summation of earthquakes, *Tectonophysics*, **359**, 29–46.
- Ritzwoller, M. H., and A. L. Levshin (1998), Eurasian surface wave tomography: Group velocities, *J. Geophys. Res.*, **103**, 4839–4878.
- Ritzwoller, M. H., A. L. Levshin, L. I. Ratnikova, and A. A. Egorkin (1998), Intermediate-period group-velocity maps across central Asia, western China and parts of the Middle East, *Geophys. J. Int.*, **134**, 315–328.
- Ritzwoller, M. H., N. M. Shapiro, M. P. Barmin, and A. L. Levshin (2002), Global surface wave diffraction tomography, *J. Geophys. Res.*, **107**(B12), 2335, doi:10.1029/2002JB001777.
- Romanowicz, B. A. (1982), Constraints on the structure of the Tibet Plateau from pure-path phase velocities of Love and Rayleigh waves, *J. Geophys. Res.*, **87**, 6865–6883.
- Segnör, A. M. C. (1984), The Cimmeride orogenic system and the tectonics of Eurasia, *Spec. Pap. Geol. Soc. Am.*, **195**, 75 pp.
- Segnör, A. M. C. (1987), Tectonics of the Tethysides: Orogenic collage development in a collisional setting, *Annu. Rev. Earth Planet. Sci.*, **15**, 213–244.
- Stevens, J. L., and S. M. Day (1985), The physical basis for m_b , M_s and variable frequency magnitude methods for earthquake/explosions discrimination, *J. Geophys. Res.*, **90**, 3009–3020.
- Stevens, J. L., and K. L. McLaughlin (2001), Optimization of surface wave identification and measurement, *Pure Appl. Geophys.*, **158**, 1547–1582.
- Stevens, J. L., D. A. Adams, and G. E. Baker (2001), Improved surface wave detection and measurement using phase-matched filtering with a global one-degree dispersion model, paper presented at the 23rd Seismic Research Review: Worldwide Monitoring of Nuclear Explosions, Natl. Nucl. Secur. Admin., Jackson Hole, Wyo.
- Stevens, J. L., D. A. Adams, G. E. Baker, M. G. Eneva, and H. Xu (2004), Improved surface-wave dispersion models, amplitude measurements, and azimuth estimates, paper presented at the 26th Seismic Research Review: Trends in Nuclear Explosion Monitoring, Natl. Nucl. Secur. Admin., Orlando, Fla.
- Tarantola, A. (1987), *Inverse Problem Theory*, 630 pp., Elsevier, New York.
- Taylor, S. R., M. D. Denny, E. S. Vergino, and R. E. Glaser (1989), Regional discrimination between NTS explosions and western U.S. earthquakes, *Bull. Seismol. Soc. Am.*, **79**, 1142–1176.
- Taylor, S. R., X. Yang, and W. S. Phillips (2003), Bayesian L_g attenuation tomography applied to eastern Asia, *Bull. Seismol. Soc. Am.*, **93**, 795–803.
- Tian, Z. Y., G. L. Chai, and Y. Z. Kang (1989), Tectonic evolution of the Tarim Basin, in *Chinese Sedimentary Basins, Sediment. Basins World*, vol. 1, edited by X. Zhu, pp. 33–43, Elsevier, New York.
- Villaseñor, A., M. H. Ritzwoller, A. L. Levshin, M. P. Barmin, E. R. Engdahl, W. Spakman, and J. Trampert (2001), Shear velocity structure of central Eurasia from inversion of surface wave velocities, *Phys. Earth Planet. Inter.*, **123**, 169–184.
- Wier, S. (1982), Surface wave dispersion and Earth structure in southeastern China, *Geophys. J. R. Astron. Soc.*, **69**, 33–47.
- Wu, F. T., A. L. Levshin, and V. M. Kozhevnikov (1997), Rayleigh wave group velocity tomography of Siberia, China and the vicinity, *Pure Appl. Geophys.*, **149**, 447–473.
- Yang, X., S. R. Taylor, H. J. Patton, M. Maceira, and A. A. Velasco (2002), Evaluation of intermediate-period (10 to 30-sec) Rayleigh-wave group-velocity maps for central Asia, paper presented at the 24th Seismic Research Review—Nuclear Explosion Monitoring: Innovation and Integration, Natl. Nucl. Secur. Admin., Ponte Vedra Beach, Fla.
- Yang, Y., and M. Liu (2002), Cenozoic deformation of the Tarim plate and the implications for mountain building in the Tibetan Plateau and the Tian Shan, *Tectonics*, **21**(6), 1059, doi:10.1029/2001TC001300.
- Yin, A., and M. Harrison (2000), Geological evolution of the Himalayan-Tibetan orogen, *Annu. Rev. Earth Planet. Sci.*, **28**, 211–280.
- Zonenshain, L. P., M. I. Kuzmin, and L. M. Natapov (1990), *Geology of the USSR: A Plate-Tectonic Synthesis*, *Geodyn. Ser.*, vol. 21, edited by B. M. Page, 242 pp., AGU, Washington, D. C.

C. J. Ammon, Department of Geosciences, Pennsylvania State University, University Park, PA 16802, USA. (cammon@geosc.psu.edu)

M. Maceira, Los Alamos National Laboratory, EES-11, Geophysics, MS D443, Los Alamos, NM 87545-0000, USA. (mmaceira@lanl.gov)

S. R. Taylor, Los Alamos National Laboratory, MS F665, Los Alamos, NM 87545, USA. (taylor@lanl.gov)

A. A. Velasco, Department of Geological Sciences, University of Texas at El Paso, El Paso, TX 79968-0555, USA. (velasco@geo.utep.edu)

X. Yang, Los Alamos National Laboratory, EES-11, MS D408, Los Alamos, NM 87545, USA. (xyang@lanl.gov)

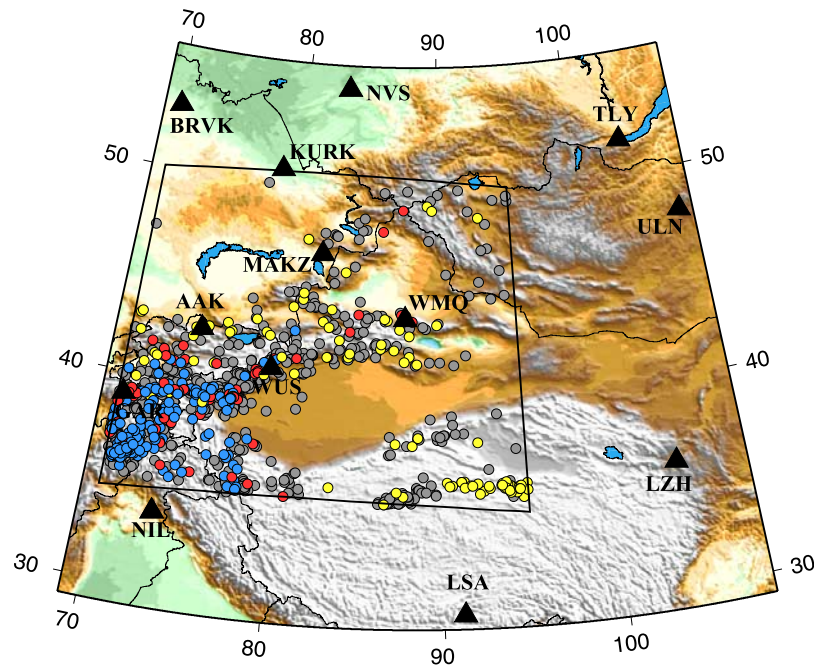


Figure 2. Topographic map of the region of central Asia under study. The black box encloses the data collection area. Events are shown as circles of different colors depending of the event depth: yellow for depths up to 30 km, red from 30 to 60 km, blue for deeper events (up to 100 km), and gray when depth is 33 km, which means that it is unknown. Stations used are shown as black triangles.

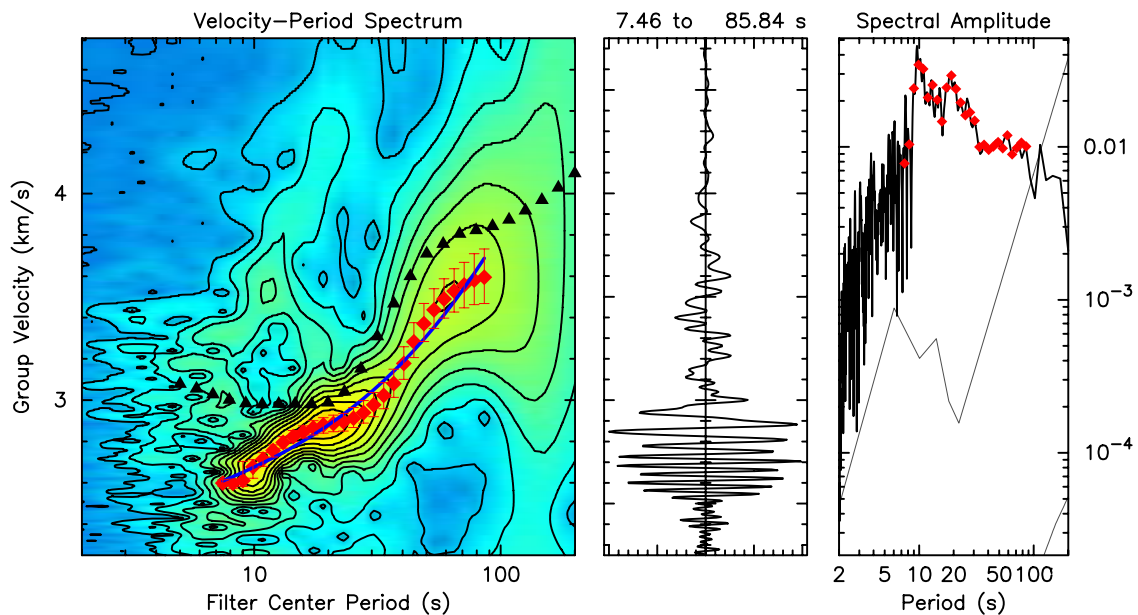


Figure 3. Display illustrating the method used to measure group velocities from an earthquake (2 May 1995, 1148:00 UT) recorded 1665.7 km far away, with an azimuth of 51.5, at station TLY, Talaya, Russia. (left) A contour diagram of the seismogram envelope. Warm colors indicate bigger amplitudes, and cold colors represent smaller amplitudes. The Rayleigh wave group velocity points are identified by red diamonds, the spline fit of the group velocities is depicted by the blue line, and the reference curve, which in this case is *Jih's* [1998] China crustal model, is plotted as black triangles. (middle) The seismogram is displayed along the group velocity axis. (right) The amplitude spectrum and the sample points along with the USGS low- and high-noise curves.

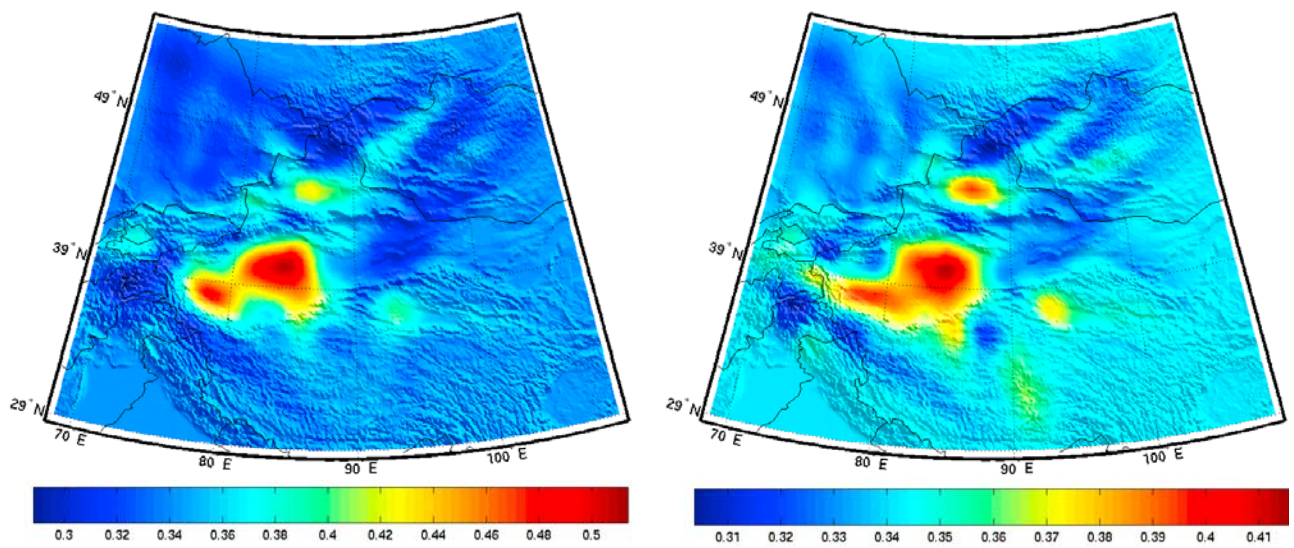


Figure 6. Rayleigh wave slowness maps computed without background model for periods of (left) 10 s and (right) 20 s. The slowness values are s/km. Note the different color scale for each map.

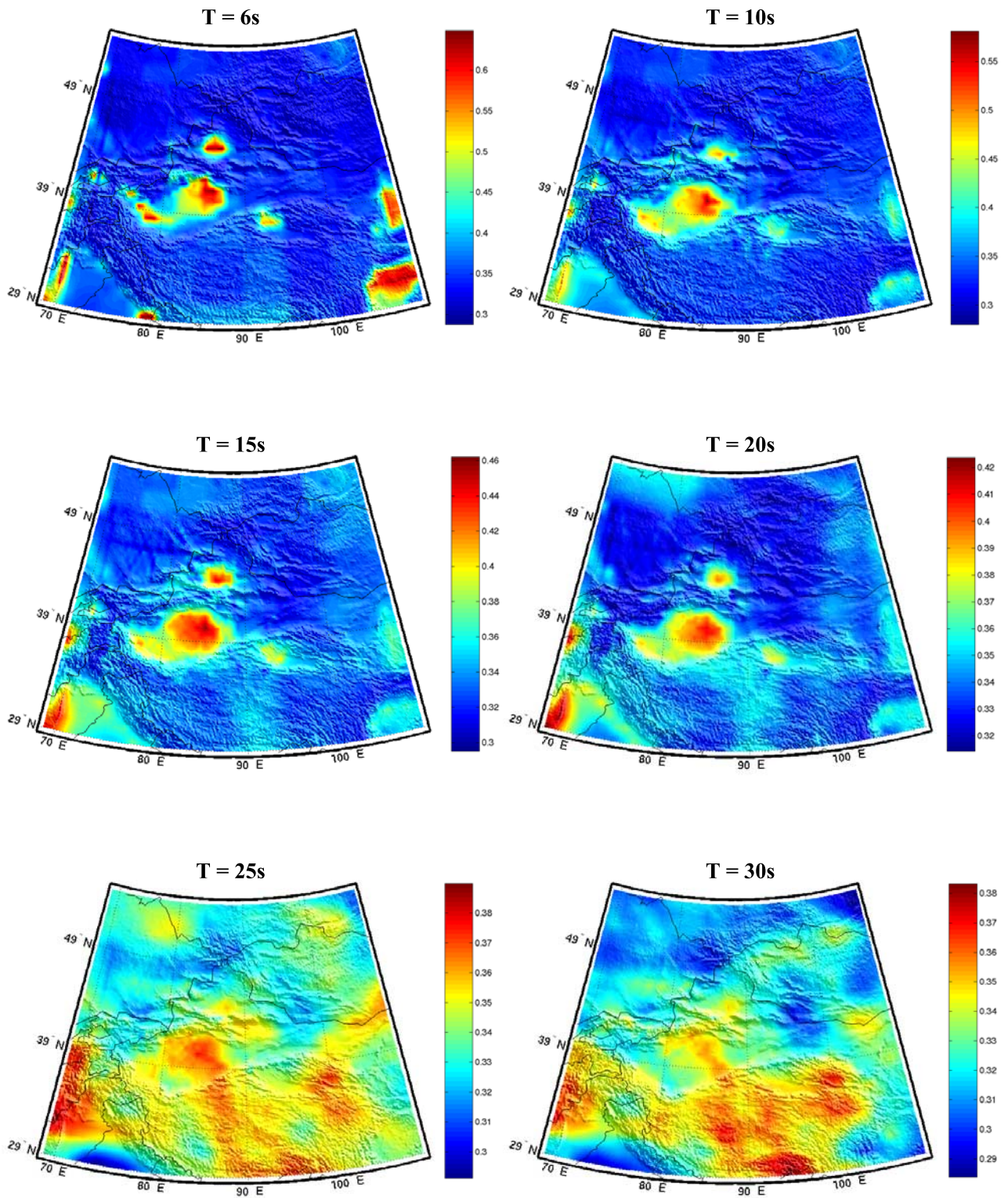


Figure 7. Rayleigh wave slowness maps for different periods. The slowness values are expressed in s/km. Note that the color scale is different for each map.

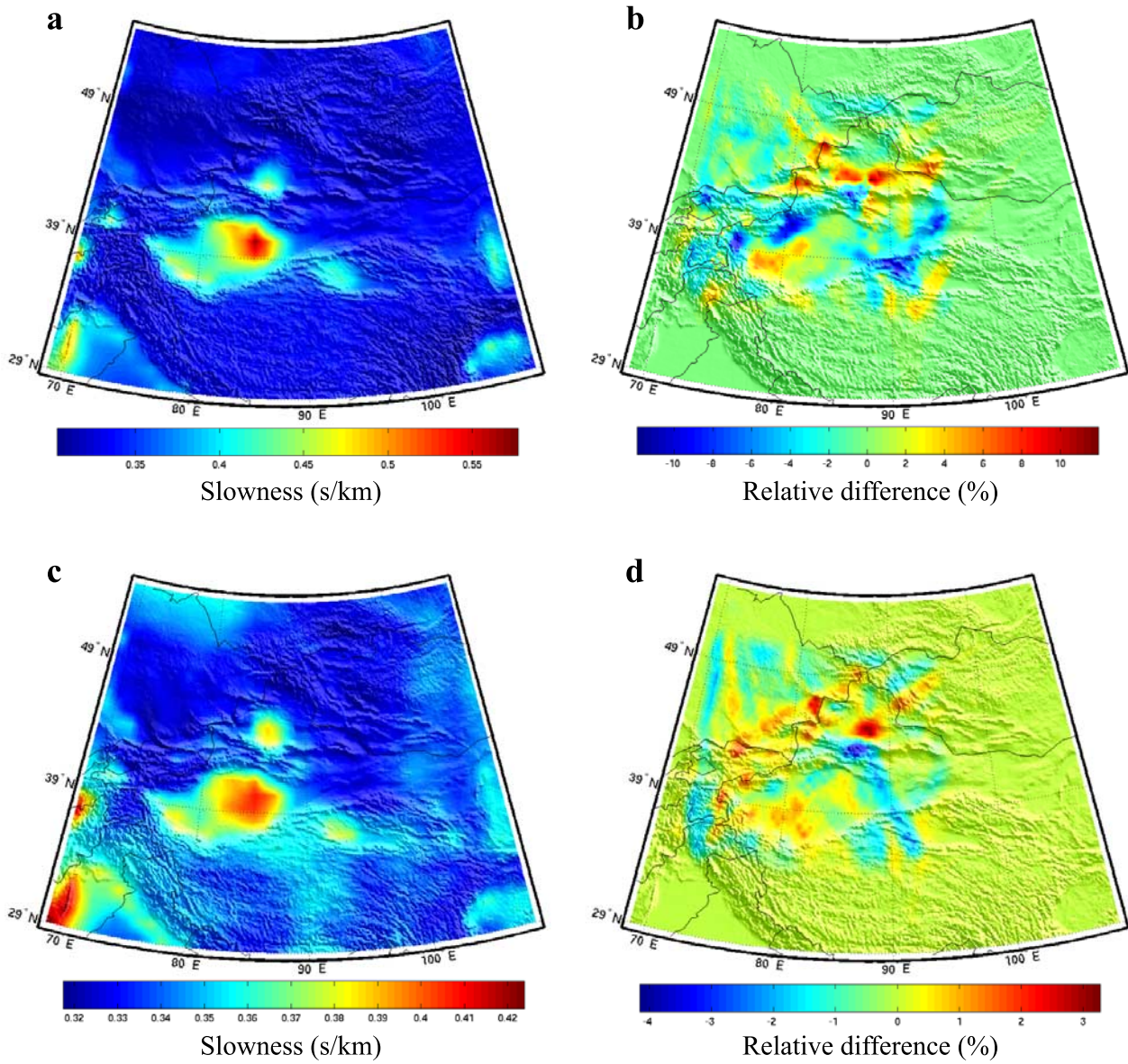


Figure 8. (a) Composite a priori map used for the tomographic inversion at 10 s. (b) Relative difference map between the refined and the reference models at 10 s. (c) Composite a priori map used for the tomographic inversion at 20 s. (d) Relative difference map between the refined and the reference models at 20 s.

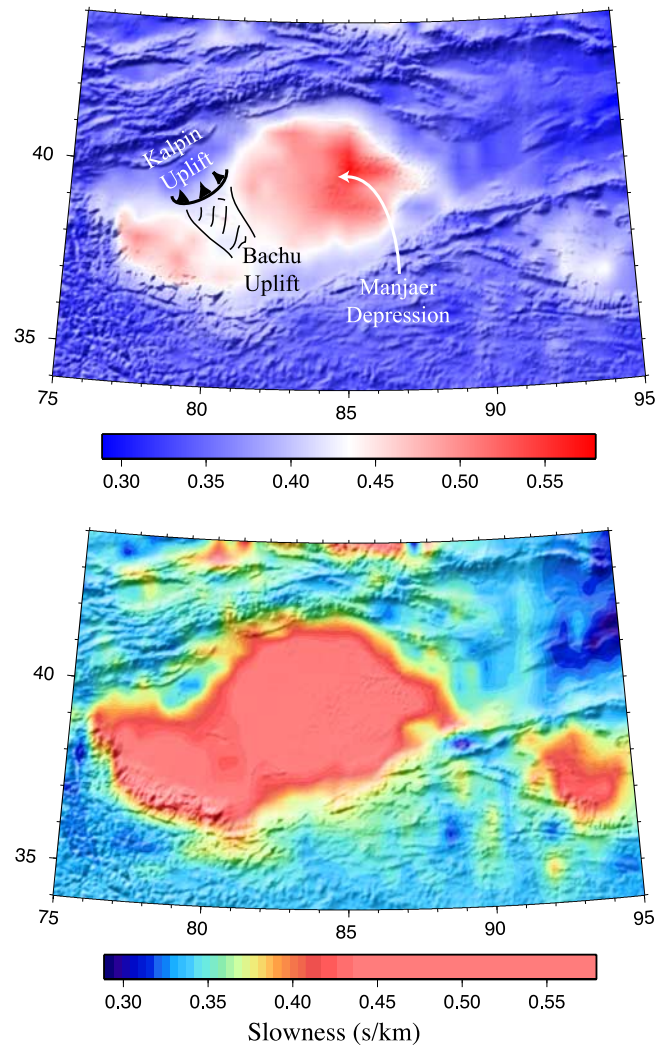


Figure 9. (top) Computed slowness model at 10 s period. Some of the main features of the Tarim basin such as the Manjaer depression and the central uplift are obvious in our refined model. (bottom) The same slowness model plotted in a different color scale to show that even some of the Cenozoic sedimentary cover north of the basin is apparent in our model.

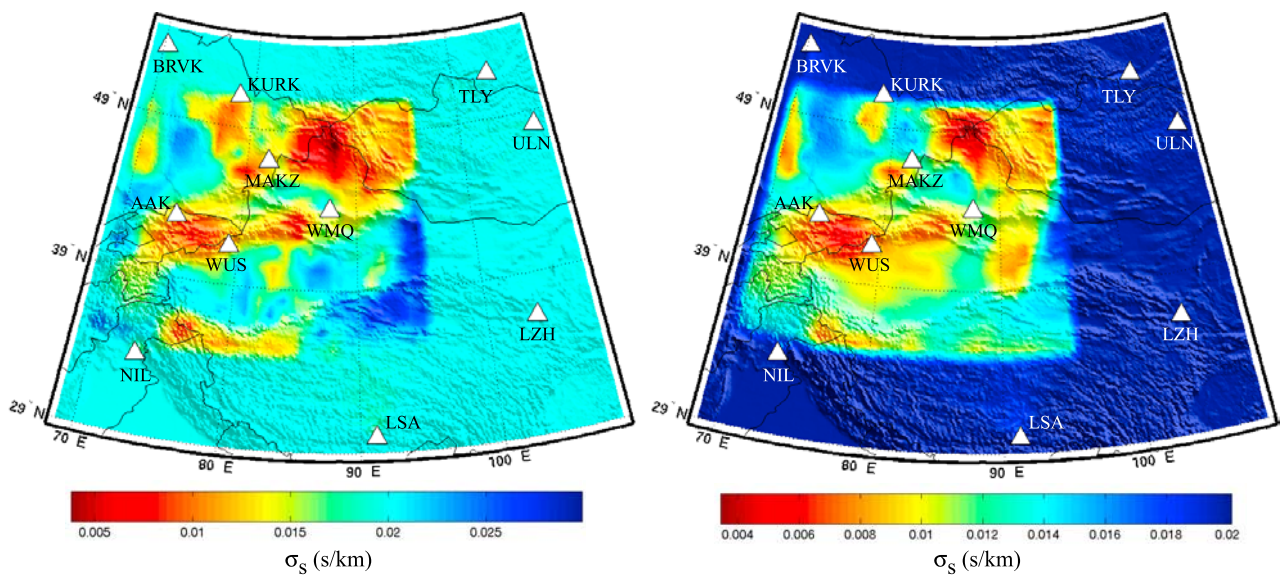


Figure 10. Standard errors on the slowness values for the tomographic model at (left) 10 s and (right) 20 s periods. Stations used are represented by the white triangles.